Optics & Laser Technology 174 (2024) 110588

Contents lists available at ScienceDirect

Optics and Laser Technology

journal homepage: www.elsevier.com/locate/optlastec

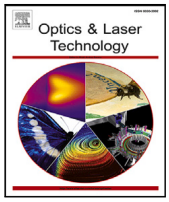

Full length article

Study of supercontinuum generation from a mode-locked Erbium-doped fiber laser based on monolayer graphene saturable absorber

D.H. Martínez-Suárez [a,b,*], M.C.S. Araujo [b], D. Steinberg [b], L.A.M. Saito [b], E.A. Thoroh de Souza [b], J.D. Zapata [a]

[a] Faculty of Engineering, Universidad de Antioquia, Cl. 67 #53 – 108, 050010, Medellín, Colombia
[b] School of Engineering, Mackenzie Presbyterian University, Rua da Consolação, 896, SP, 01302-907, São Paulo, Brazil

ARTICLE INFO

Dataset link: SC-JOLT_110588

Keywords:
Supercontinuum generation
Monolayer graphene
Ultrashort pulses
Erbium-doped fiber laser

ABSTRACT

We study the supercontinuum (SC) generation from a passively mode-locked erbium-doped fiber laser (ML-EDFL) using two different samples of monolayer graphene saturable absorber (SA) onto the side-polished surface of a D-shaped fiber, characterized with 98% and 65% polarization dependent loss (PDL), respectively. By using the first 98% PDL graphene SA (setup-1), output pulse spectral profile with 11.6 nm bandwidth was obtained from the ML-EDFL and subsequently amplified using an erbium-doped fiber amplifier (EDFA) to pump 2-m highly nonlinear fiber (HNLF) and 5-m ZBLAN lengths, both fibers operating at the normal dispersion regime, which resulted in individual SC generation of 350 and 245 nm, respectively. Furthermore, the EDFA was spectrally characterized by observing their SC blue shift of the central wavelength, reaching a value of 6.9 nm at 12 dB due to dispersion gain. With the second 65% PDL graphene SA (setup-2), we could generate SC with 227 and 351 nm bandwidths using 0.5 and 2 m HNLF lengths, respectively. Because the two SC setups were highly dependent on the polarization state of the input pulse, we optimized the SC generation from setup-2 using an external polarization controller (PC), which allowed us to adjust both the spectral brightness and the broadening of the SC.

1. Introduction

In the last decade, mode-locked sources using rare-earth-doped fiber lasers have attracted interest due to their excellent potential to generate new ranges of photonic and biomedical applications [1]. Particularly in medicine, a wide technological demand is driven toward detecting tissues, analytes, or biomarkers for the prognosis or diagnosis of different pathologies, which has prompted the development of broadband sources in the near and mid-infrared spectral regions [2].

The importance of studying the infrared spectral region, especially the molecular fingerprint region, is explained by the characteristic vibrational frequencies of molecular bonds, leading to their resonant absorption peaks in these wavelengths [3], which is the foundation for molecular spectroscopy [4], bio-diagnostic [5] and laser surgery applications [6]. Therefore, mode-locked fiber lasers have been playing a central role in developing these technologies, attributed to their properties of compact structure, good flexibility, and low cost [7].

Most ultrafast laser systems employ a mode-locking (ML) technique by incorporating a nonlinear optical element called saturable absorber (SA) [8–10]. In the past decades, the dominant technology was focused on semiconductor-based SA mirrors (SESAM) [11] and carbon nanotubes [12]. However, these have a narrow tuning range, high non-saturable losses, low damage thresholds, advanced fabrication techniques, and packaging [13]. For this matter, graphene has emerged as a potential candidate with excellent transport phenomena characteristic of 2D Dirac fermions [14] and also remarkable optical properties, including its high transmittance ($T \approx 1 - \pi\alpha = 97.7\%$), low nonsaturable losses, ultrafast relaxation time [15], broadband saturable absorption (Pauli blocking) [16], being the only material produced and obtained by all known methods (mechanical exfoliation, chemical vapor deposition — CVD, liquid phase exfoliation — LPE), and compatible with all fiber systems (optical fiber connector tip, D-shaped fiber, tapered fiber, photonic crystal fiber, etc.) for ultrafast fiber lasers applications [17–25].

Allied with ML fiber lasers, the supercontinuum (SC) generation have evolved in the last decades to become a mature laser technology [26–30]. Several soft glasses based on chalcogenide (As_2S_3, As_2Se_3, GeAsSe), tellurite (TeO_2), telluride (GeTe, GeAsTeSe), heavy-metal oxide ($PbO-Bi_2O_3-Ga_2O_3-SiO_2-CdO$), and ZBLAN ($ZrF_4-BaF-LaF_3-AlF_3-NaF$) [31–33], have been used to design highly nonlinear infrared

* Corresponding author at: Faculty of Engineering, Universidad de Antioquia, Cl. 67 #53 – 108, 050010, Medellín, Colombia.
E-mail address: dhumberto.martinez@udea.edu.co (D.H. Martínez-Suárez).

https://doi.org/10.1016/j.optlastec.2024.110588
Received 11 March 2023; Received in revised form 26 December 2023; Accepted 9 January 2024
Available online 23 January 2024

fiber and efficient supercontinuum generation in the mid-IR region up to 14 μm using chalcogenide optical fibers and up to 16 μm using telluride fiber [34].

On the other hand, there is a growing interest in the applications of 2D materials driven by their optical and electrical properties, such as graphene, black phosphorus, transition metal dichalcogenide (MoS_2, WS_2), topological insulators (Bi_2Te_3, Bi_2Se_3, Sb_2Te_3), MXenes, graphitic carbon nitride, and metal-organic framework [35–38]. According to references, these materials can increase the performance of the SC generation [39]. Also, computer simulations have demonstrated a multi-octave broadening of the SC spectrum ranging from 1.5 to 25 μm using graphene waveguides and generating plasmonic modes [40]. This is the ideal scenario for SC engineering by studying the solitons fission using dispersive wave radiation in the anomalous dispersion region [41].

In this work, we studied the SC generation from two mode-locked Erbium doped fiber lasers (EDFL) based on monolayer graphene as saturable absorbers onto D-shaped fibers. From these lasers, different soliton profiles were used as input pulse seeds to analyze the spectral broadening dynamics of SC. Firstly, the EDFA was spectrally characterized by analyzing its bandwidth and blue shift parameters of the output spectrum as a function of the amplifier gain, reaching a maximum center wavelength shift of 6.9 nm at 12 dB. Two setups were used to analyze the SC spectrum broadening. In the first configuration (setup-1), output pulses from an ML-EDFL based on a monolayer graphene SA/D-shaped fiber sample with 98% polarization-dependent loss (PDL) were used to pump 2-m HNLF and 5-m ZBLAN lengths. In the second configuration (setup-2), the same experiment was repeated using output pulses from an ML-EDFL based on a monolayer graphene SA/D-shaped sample with 65% PDL to pump 0.5 and 2-m HNLF lengths. In this last setup, an external polarization controller (PC) was additionally used to adjust the polarization state of the input pulse that pumped the HNLF. Considering the 20-dBm spectral width, we found the maximum SC spectrum broadening of 350 and 245 nm from setup-1 using a 11–13 dB amplifier gain range for HNLF and ZBLAN fibers, respectively. From setup-2, SC generation dependence on the input polarization state was tested, and different spectral profiles were generated. As a result, broadened SC spectra of 227 and 351 nm were obtained for 0.5-m and 2-m HNLF lengths, respectively, exhibiting a spectral brightness difference of (5.0 ± 1.8) dBm from each other.

2. Experimental section

For the study of SC generation, we used different seed lasers (EDFL) based on two monolayer graphene samples as SA, referred as G_{98} and G_{65}, according to their polarization dependent loss (PDL) calculated parameters of 98% and 65%, respectively (see https://doi.org/10.1016/j.optlastec.2024.110588Supplementary Material).

2.1. EDFL setup

The experimental setup of the EDFL source is illustrated in Fig. 1a. The EDFL ring cavity consists of 0.75-m long Erbium doped fiber as the gain medium, pumped by a 980-nm diode laser (CLD1015) via a hybrid 980/1550 nm wavelength division multiplexing (WDM)/isolator component (ensuring unidirectionality of 1550-nm signal at co-propagating configuration), a polarization controller (PC), a 10/90 optical output coupler (OC), and the monolayer graphene SA onto D-shaped fibers (G_{98} and G_{65}, both connected at A and B points), resulting in a total cavity lengths of 4.14-m and 4.01-m with net anomalous dispersion of +33.8 and +32.7 fs/nm, respectively.

Monolayer graphene samples were obtained from chemical vapor deposition (CVD) method and wet transferred onto the polished surface of D-shaped fibers [42]. As shown in Fig. 1b, we characterized the mean output power of both $EDFL_{98}$ and $EDFL_{65}$ as a function of the pumping power in steps of 1.2 mW to find the minimum power to generate the mode-locking regime. As result, mean powers from 0.8 to 2.7 mW (corresponding to 79–267 mW pump power range (blue line)), and 0.3 to 0.6 mW (corresponding to 148–267 mW pump power range (red line)) were obtained, respectively, also showing lower efficiency curves due to graphene SA high insertion losses (~8 dB, Figure S6).

The variations in the output power curves (also represented by the standard deviation — Std (shaded area)), corresponds to transient states between the continuous wave (CW) and ML, the last being recoverable by the slight adjustment of the PC paddles. This characterization is a measurement of the ML regime stability as the pumping power increases, having better behavior for the $EDFL_{98}$, while the $EDFL_{65}$ behaves more unstable below 220 mW. Above 150 mW, the $EDFL_{98}$ presented a step-like behavior in the output power, which was experimentally related to transitions between conventional and bound-state solitons from the spectrum.

Fig. 1c and d show the spectral pulse profiles of the mode-locked $EDFL_{98}$($EDFL_{65}$) with 14.1 nm (18.0 nm) bandwidths, centered at 1559 nm (1565 nm), respectively, both obtained at pump power of 245 mW. Their spectra showed different soliton pulses: Kelly ($EDFL_{98}$) and bound state ($EDFL_{65}$) profiles, both fitted by $sech^2$ model. Fig. 1e,f show the associated polarization states, particularly with right ($EDFL_{98}$) and left ($EDFL_{65}$) elliptical rotations, which depend on the mode-locked soliton profile inside these cavities (the parameters of these polarization states are found in table S2). These pulses were amplified into the EDFA and then used to pump highly nonlinear fibers for SC generation (Section 3).

2.2. Characterization of the pulse spectrum as a function of the EDFA gain

The mode-locked $EDFL_{98}$ pulses were amplified through an EDFA (MultiPad MPD 1200, Padtec), and their output power was varied by modifying the amplifier gain using a device communication software. Fig. 2 illustrates the output optical spectrum behavior as a function of amplifier gain (linear scale). The spectra have been shifted vertically to evaluate the differences as the pulse was amplified qualitatively. This characterization shows the spectral evolution as a function of the amplifier power's increase. As gain increases, the pulse increases its spectral amplitude, and a blue shift from the reference wavelength appears, as emerged by the frequency dependence of the gain dispersion.

Physically, the shift of the pulse spectrum from the erbium gain peak reduces its gain experienced by the center frequency of the input spectrum [43]. Thus, spectral components (lasing lines located mainly at 1546 nm, Kelly sidebands) located near the peak are more amplified and experience higher amplification than the rest of the spectrum, becoming the highest amplitude peak at 16 dB. Qualitatively, the amplifier tries to pull the pulse spectrum toward the erbium gain peak, decreasing the Raman-induced frequency shift of solitons.

This can also be understood by analyzing the non-uniform absorption/emission spectrum of an erbium-doped fiber (as gain medium of EDFA). The different spectral components associated with the input seed pulse spectrum into the EDFA will not be amplified in the same way, inducing a frequency dependence of the gain or gain dispersion. As the gain increases from 0 to 12 dB, the gain experienced by the shorter wavelength components of the pulse spectrum central wavelength will be larger than those of longer ones, experiencing a non-uniform increase in their spectral power due to gain dispersion and shifting the center frequency towards the erbium gain peak, i.e. blue shift. Therefore, this phenomenon will depend on the characteristics of the spectral shaping of the input pulse into the EDFA. Fig. 3 shows the blue shift of the spectrum's center wavelength, reaching a shift of 6.9 nm at 12 dB, and its corresponding spectral power.

As the amplifier gain increases, new spectral components are also amplified due to: (1) spontaneous emission, since this is one of the noise sources in amplifiers, and (2) modulation instability (MI). In addition, spontaneous emission adds broadband noise to the amplified signal, which can seed the growth of MI and be amplified via induced

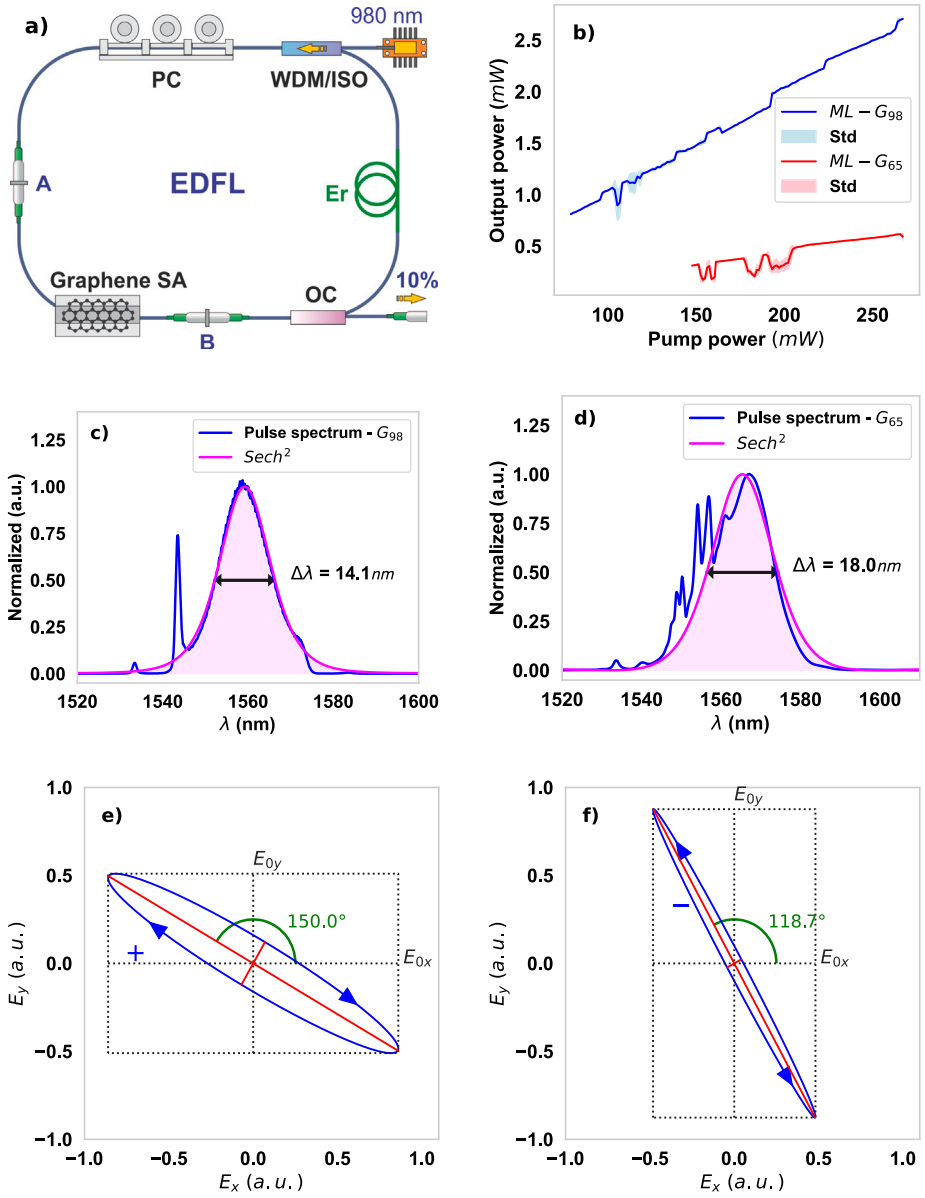

Fig. 1. EDFL setup: (a) EDFL experimental setup, (b) pumping power vs. mean output power of ML regime, (c, d) linear spectrum of ML regime fitted by squared hyperbolic secant (normalized units), (e,f) polarization ellipses of the output vector solitons, for monolayer graphene samples with 98% and 65% PDL (G_{98} and G_{65}), respectively.

MI. The noise amplification broadens the signal spectrum, and such effects become more robust when a low-power signal is amplified by a significant factor, as in the case of 16-dB gain. On the other hand, gain dispersion can influence the reduction of the spectral bandwidth, obtaining a minimum value of 6.3 nm (FWHM) at 6 dB. For gain values higher than 12 dB, the spectral amplitude of the pulses is comparable to the other amplified frequencies in the baseline near the input spectrum, in which the single soliton profile is no longer dominant.

For verifying the noise of the two systems, we measured the signal-to-noise ratio (SNR) of both input and output pulses of the EDFA at 16 dB (Fig. 4) using an 1.2 GHz InGaAs photodetector (DET01CFC/M) connected to a radio frequency (RF) receiver (RTL2832u). These results are summarized in Table 1, showing 6.6 and 4.1 dB of noise figures values for $EDFL_{98}$ and $EDFL_{65}$, respectively. It is interesting to observe the behavior of the RF spectrum obtained for $EDFL_{65}$ at the entrance of the EDFA (Fig. 4b) showing the presence of another active band at 37.92 MHz, also amplified by the EDFA.

Table 1
Characterization of the EDFA noise figure.

	Frequency (MHz)	SNR_{in}	SNR_{out}	Noise figure
G_{98}	36.21	71.7	78.3	6.6
G_{65}	37.42	31.8	35.9	4.1

3. Results and discussions

3.1. SC generation using HNFL and ZBLAN fibers

We used 2-m long highly nonlinear fiber (HNFL, Thorlabs) and 5-m long ZBLAN fiber (Zirconium Fluoride — ZrF4, Thorlabs). According to the manufacturer's data, the parameters of these fibers are depicted in Table 2.

The dynamics of nonlinear phenomena in the SC generation are highly dependent on the distance between the center wavelength of the input spectrum (λ_c) and the zero-dispersion wavelength (ZDW), which

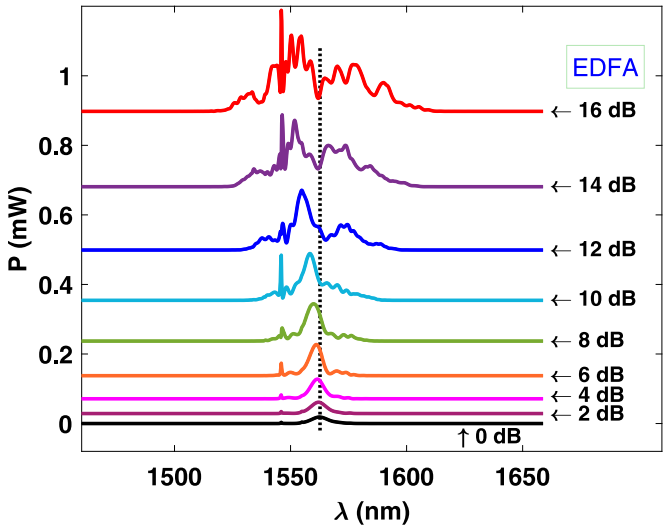

Fig. 2. Spectrum characterization as a function of EDFA gain (linear scale). The dashed vertical line represents the reference wavelength of the unamplified input pulse (see Fig. 1-c).

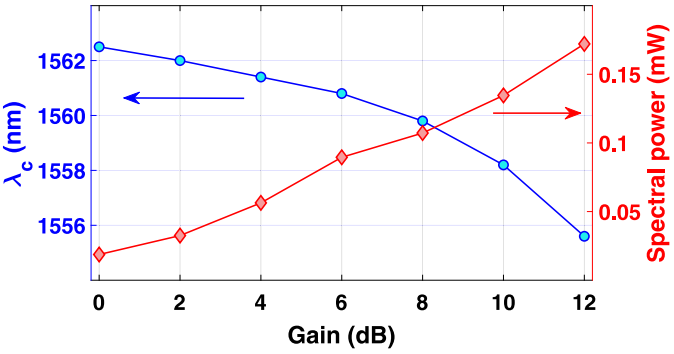

Fig. 3. Blue-shift pulse's center wavelength and corresponding power from 0 to 12 dB gain values.

Table 2
Parameters of nonlinear fibers at 1550 nm.

Nonlinear fiber	Attenuation (dB/km)	Dispersion (ps/km.nm)	Dispersion slope (ps/nm^2 km)
HNLF	<0.9	−0.98	0.005
ZBLAN	<50	−2.06	0.039

determines the spectral characteristics of SC. Fig. 5 illustrates the fiber's dispersion curves, showing the spectral region of the input pulses in the marked area (pink area).

In these curves, we observed that the ZBLAN's ZDW fiber (1616 nm) is 60 nm far from the input spectrum center wavelength localized at the normal dispersion regime. HNLF's ZDW is not reached in this analysis window since its dispersion curve has a flatter behavior. Under these conditions, self-phase modulation (SPM) will predominate in the pulse spectral broadening due to induced linear chirp at a normal dispersion regime as the pulses propagate along the fiber with the same sign of the nonlinearity chirp. We studied the SC spectral broadening from HNLF and ZBLAN fibers concerning the amplified output pulses using the first SC setup (setup-1, employing $EDFL_{98}$), as shown in Fig. 6a. Fig. 6b illustrates the output power behavior as a function of amplifier gain before (blue curve) and after the nonlinear fibers (red/pink curves). From the curves, we observed that the saturation region of the amplifier could not be achieved using the maximum experimental power range.

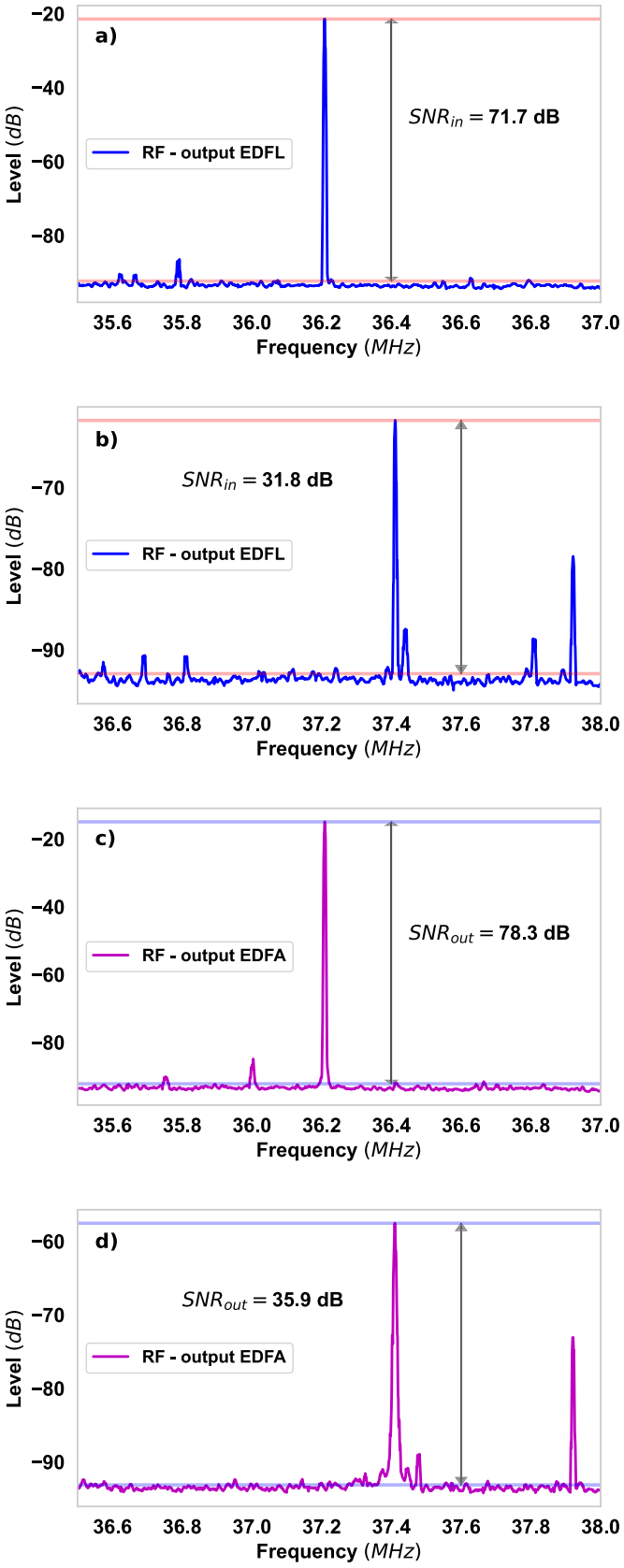

Fig. 4. RF spectra at the (a, b) input (SNR_{in}) and (c,d) output of the EDFA (SNR_{out}) at 16-dB, using samples G_{98} and G_{65}, respectively.

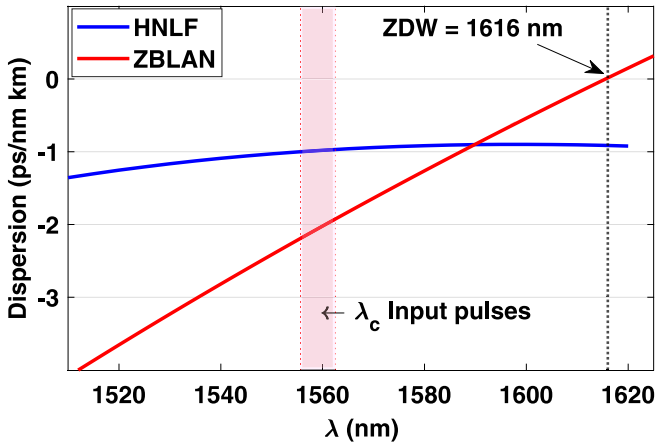

Fig. 5. Dispersion curves of nonlinear fibers. ZBLAN's ZDW fiber at 1616 nm.

With these data, we found an experimental attenuation of $(21.7 \pm 0.3) \times 10^2$ and (88.3 ± 9.6) dB/km, for 2-m long HNLF and 5-m long ZBLAN, respectively. These results differ from those in Table 1, especially for the HNLF due to the coupling losses. Fig. 7a is depicted the output spectrum of 2-m long HNLF as a function of amplifier gain from 0 to 12 dB (logarithmic scale), showing the spectral broadening as the input spectrum power increases. Similarly, Fig. 7b also shows the output spectrum from ZBLAN as a function of amplifier gain from 0 to 13 dB. The occurrence of the spectral peaks are mainly due to the SPM, which is a predominant nonlinear optical phenomenon in the SC generation related to the pulse propagation at normal dispersion regime in both HNLF and ZBLAN fibers. One of the main characteristics of SPM is the frequency chirp dependence on time, causing the pulse to have the same instantaneous frequency at different points. This can be interpreted as waves with the same frequency but different phases, which can interfere destructively or constructively with each other according to their relative phase difference, resulting in a multi-peak structure. The greater nonlinear phase shift produced by SPM, the greater the number of ripples in the spectrum.

A common approach to characterize the spectral broadening of SC is measuring its bandwidth at 20-dB spectral power difference, as defined by the wavelength range in which the power level exceeds 1% of the peak value [44]. Extrapolating this approach to characterize the

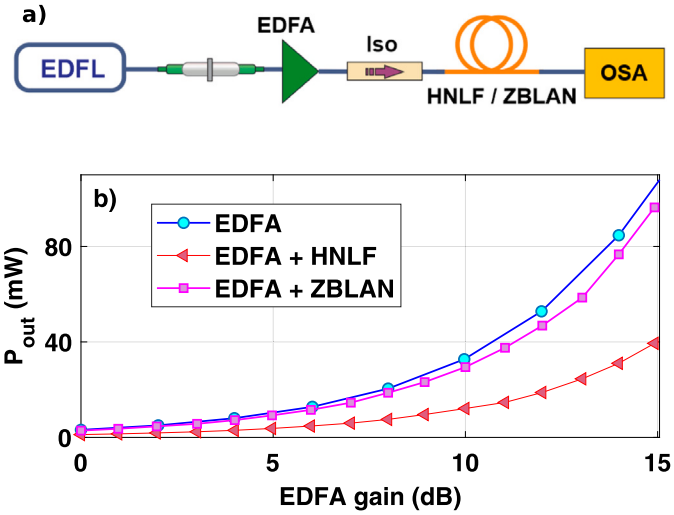

Fig. 6. (a) Setup-1 for SC generation and (b) output power as a function of gain from EDFA, 2-m long HNLF, and 5-m long ZBLAN fibers.

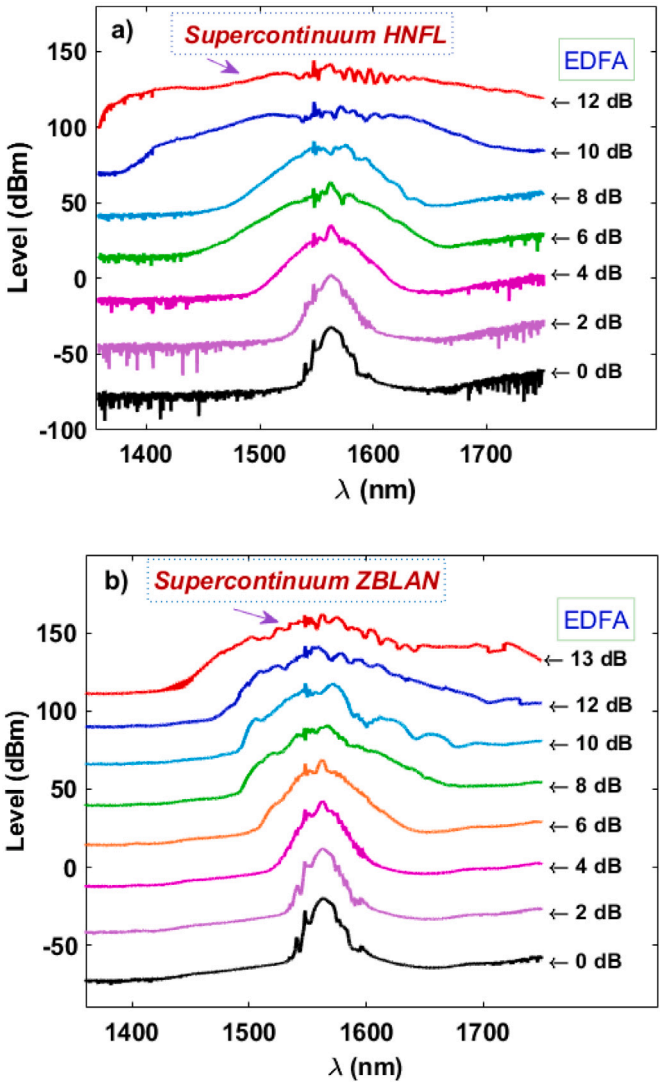

Fig. 7. SC output spectra generation as a function of the input pulse spectrum power obtained for (a) HNFL and (b) ZBLAN fibers at logarithmic scale.

spectral broadening of Fig. 7, the bandwidth was measured at 20-dBm as a function of the EDFA gain, obtaining Fig. 8. It is important to highlight that the configuration of the pulse spectrum seed in the EDFA and subsequently both nonlinear fibers is the same, therefore Fig. 7 shows us the response of the nonlinear fibers for each pulse shape (see Fig. 2) after being amplified. Apart from the change of the polarization state induced by the EDFA, the SPM depends on both the pulse shape and its initial chirp in the amplification process. Therefore, we can associate the maximum SPM broadening with the maximum generation of positive chirp, which will depend on the parameters of the nonlinear fibers and the pumping power of the EDFA.

Fig. 8 shows that the maximum broadening for the HNLF occurs at 11-dB, according to the metric used. Unlike 2-m long HNFL, the maximum spectral broadening was achieved at 13 dB gain for ZBLAN. In the same line, we studied the spectral power around the central wavelength of the input pulse (centered at approximately 100 nm spectral range). Considering this fact, we could quantify the spectral broadening behavior as a function of the area under the curve (spectral density) in the lateral regions of the spectrum (Fig. 9a,c). This allowed us to find the amplifier gain value responsible for generating the most symmetrical spectral bandwidth observed in the OSA window.

According to Fig. 9b, the maximum area under the curve at 12-dB was obtained simultaneously at both right and left regions for

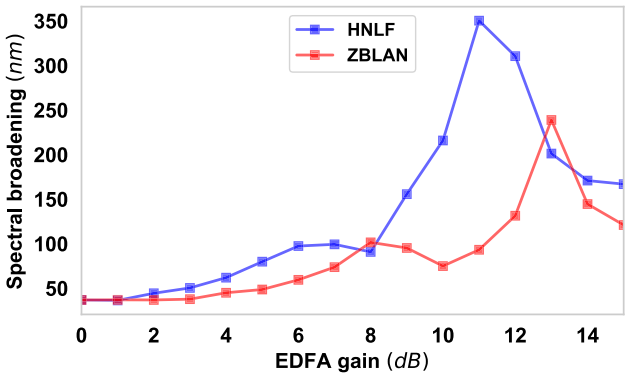

Fig. 8. Spectral broadening at 20 dBm as a function of EDFA gain.

HNLF, tending to be symmetrical concerning the input pulse spectrum. For ZBLAN (Fig. 9d), the maximum broadening was achieved at 13-dB, presenting an asymmetric spectral behavior with respect to the input pulse spectrum and better performance at low frequencies. These results showed that the spectral broadening decreased for higher gains (≥11 dB). Comparing this result with those of Fig. 8, the SC with high symmetry was separated from the maximum broadening by 1-dB of gain in the EDFA.

Fig. 10a compares the SC maximum spectral broadening generation at 20-dBm obtained for both fibers with the input pulse spectrum (11.6 nm of bandwidth, blue line). Similarly, the spectral broadening at 30-dBm was measured to quantify the SC bandwidth, where significant variations were observed (Fig. 9b,c) far from the central region that concentrates most of the spectral power. Results of these measures are summarized in Table 3. According to this table, SC spectral bandwidth obtained from HNLF (350-nm, red line) was broader than ZBLAN (245-nm, pink line) at 20-dBm spectral power difference, but exhibited a lower mean spectral brightness of 10.4-dBm in that range. Measurements at 30 dBm were limited to our OSA equipment's maximum wavelength span range (600–1750 nm).

Table 3
SC parameters obtained from setup-1.

Fiber	Length (m)	At 20-dBm	At 30-dBm	Output power (mW)
HNLF	2	350 nm	>386 nm	18.8
ZBLAN	5	245 nm	>286 nm	58.6

3.2. SC generation dependence on the input polarization state in HNLF from ML EDFL

To study the SC spectrum broadening as a function of the input pulse polarization state into HNLF, we repeated the measurements by changing the position of the PC paddles inside the EDFL in the setup-1 to obtain ML with different spectral characteristics in terms of bandwidth, Kelly sidebands and central wavelength (Fig. 11). Depending on the PC states, the loss and spectral broadening of the SC can be more significant for some configurations than others. This suggests a high dependence of the SC generation on the input spectrum polarization state before entering the EDFA and subsequently to the HNLF.

Fig. 11a shows the mode-locking regimes obtained with different PC configurations of the mode-locked EDLF. By moving the paddles, the intracavity polarization state was modified, changing the absorption of TE and TM modes in the monolayer graphene (physical SA) and nonlinear polarization rotation — NPR (artificial SA) mechanism, and consequently the gain/loss balance. This determines the net gain window of the hybrid system (graphene+NPR) and the number of phase-oscillating modes, thus affecting both the bandwidth and the central wavelength of pulse spectrum. The central wavelength and

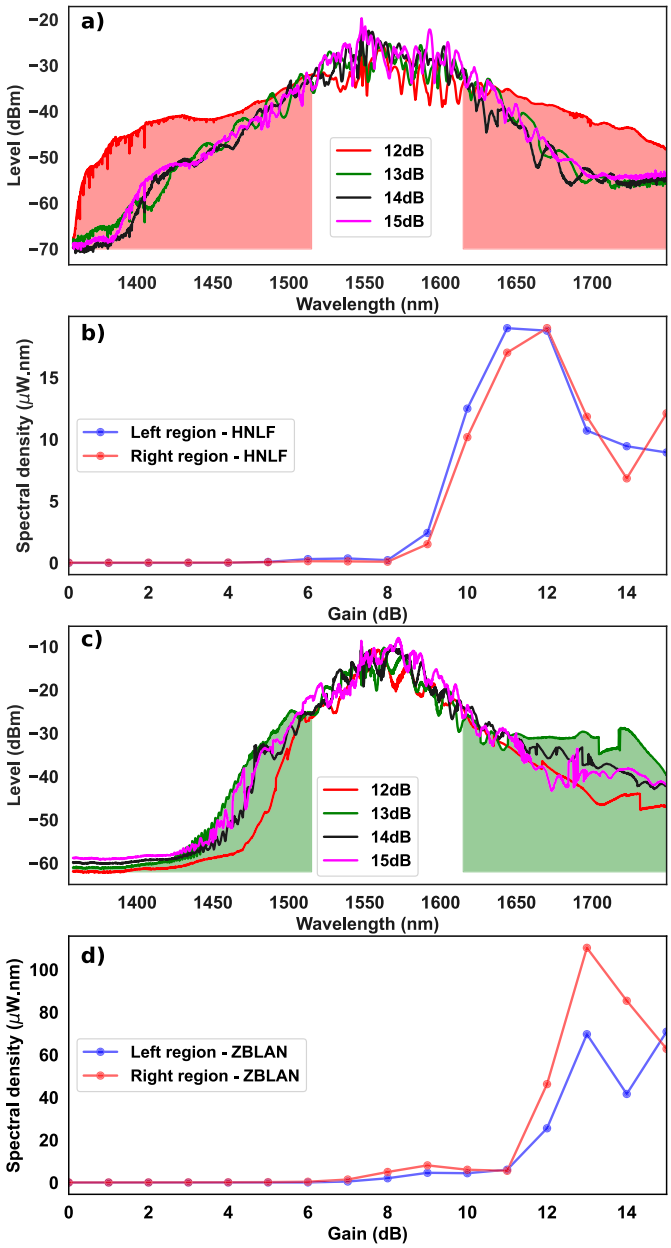

Fig. 9. Spectral density analysis outside the central region (100-nm window). (a) and (c) represent the spectral broadening from 12 to 15 dB gain range for HNLF and ZBLAN fiber, respectively; (b) and (d) represents the spectral density as a function of EDFA gain in the left and right spectrum regions (outside the central region) for HNLF and ZBLAN fiber, respectively.

bandwidth of the obtained pulse spectra are shown in the Table 4 (polarization states associated with these pulse spectra seeds can be seen in the table S3). SC generation results obtained with these ML regimes are shown in Fig. 11b.

Table 4
Input pulse spectra parameters.

Spectrum	Central wavelength (nm)	Bandwidth (nm)
1	1561.6	11.6
2	1562.4	15.7
3	1559.6	13.4
4	1560.3	15.0

3.3. SC generation as a function of the HNLF length and external PC

This study used a second SC setup (setup-2, Fig. 12) based on a monolayer graphene/D-shaped fiber sample with 65% PDL as SA

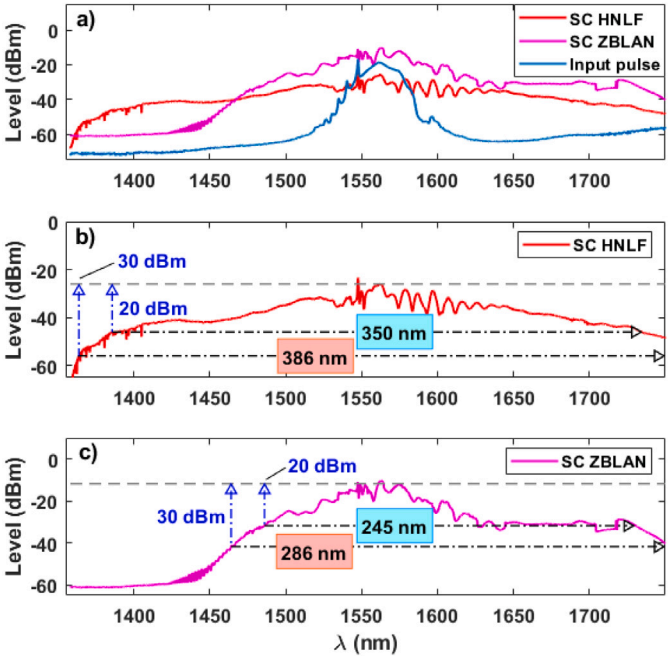

Fig. 10. SC generation spectra at log scale. (a) SCs comparison is relative to the input spectrum (blue line) and their estimated spectral broadening obtained with (b) HNFL and (c) ZBLAN.

($EDFL_{65}$). The EDFA gain was set at 15 dB. A second PC (PC_2) was inserted before the amplifier to mitigate the polarization state influence on spectral broadening (Fig. 11-b). The input pulse spectrum used in this configuration is shown in Fig. 13a, showing a 0.6 mW mean power and characteristic frequency distribution profile of a bound state soliton pulse [45]. By manually adjusting the PC_2 paddles, we could observe significant changes in both spectral broadening and brightness of generated SC. These results are shown in Fig. 13b,c using 10 and 5 spectra regarding spectral variations for 2 and 0.5-m HNLF lengths, respectively. The dependence of SC generation on the HNFL length was compared in Fig. 13d using the mean spectra for each nonlinear fiber length. According to the variations in spectral power (Fig. 13b,c), an mean standard deviation of 1.3 and 0.5 μW for 2 and 0.5-m HNLF lengths, respectively, was measured.

Spectral bandwidth measurements of SC at 20-dBm and 30-dBm are shown in Table 5. As observed, the SC generation using 2-m HNLF performed the best bandwidth results at both 20-dBm (351-nm) at 30-dBm (402-nm) (see Fig. 13d) and a (5.0 ± 1.8) dBm higher spectral brightness than that with 0.5-m HNLF. This last tends to increase the broadening below 30-dBm slightly.

It is essential to notice that the PC_2 insertion allowed us to adjust the input polarization states and adjust the SC spectral broadening. By comparing the 2-m HNLF results from Tables 3 and 5, we observed that the spectral broadenings are similar in both setups (~350 nm at 20-dBm), with the difference that the pulse spectrum of setup-2 has a lower mean power, which showed the direct influence of both input spectral profile, polarization state, and external PC_2 in the resulted SC, thus allowing the system to operate at higher EDFA gains. For comparison, we summarized some of the reported works in terms of seed EDFLs

Table 5
SC bandwidth measurement of setup-2.

Fiber	Length (m)	At 20-dBm	At 30-dBm
HNLF	2	351 nm	>402 nm
	0.5	230 nm	399 nm

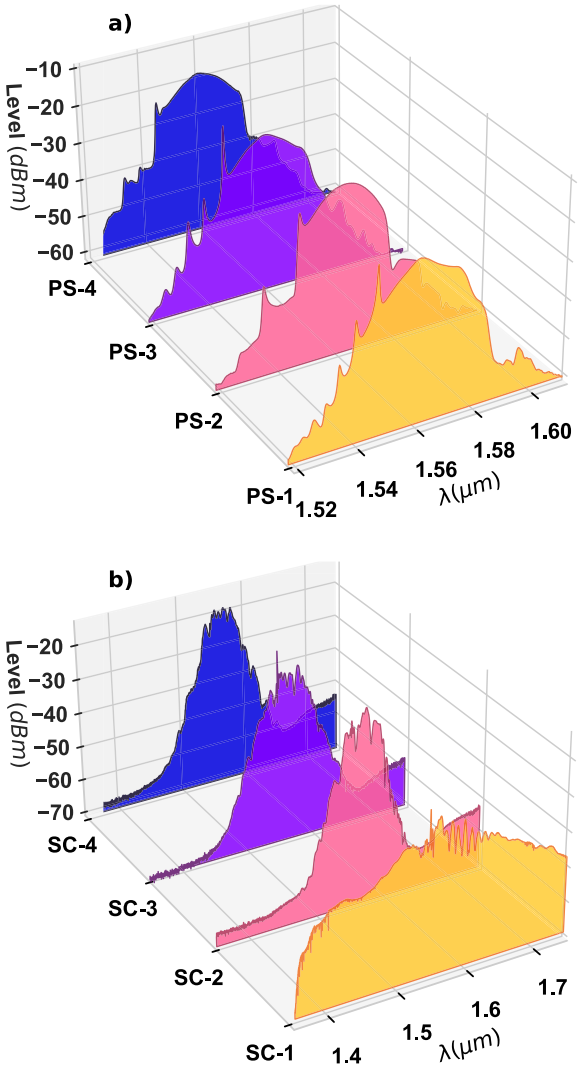

Fig. 11. (a) Pulse spectra (PS) and (b) spectral broadening (SC) obtained with different polarization states, respectively.

(SA type, fiber configuration, laser bandwidth) and their SC generation (nonlinear fiber, maximum SC bandwidth) parameters in Table 6.

Among the references in Table 6, we verified that (1) we have been the only research group to report the use of seed mode-locked EDFL based on monolayer graphene onto D-shaped fiber pulses for studying the SC generation [61]; (2) most of the works used only conventional Kelly soliton as seed pulses for SC generation and (3) there are no

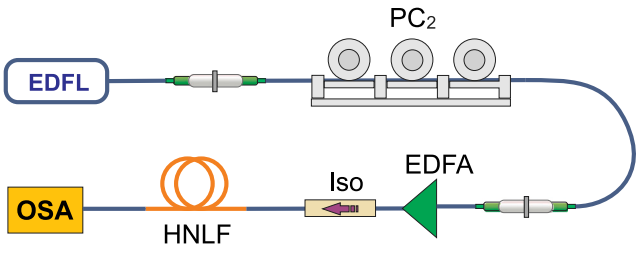

Fig. 12. Setup-2 for SC generation: SC generation configuration using another PC to adjust the polarization state before entering the HNLF.

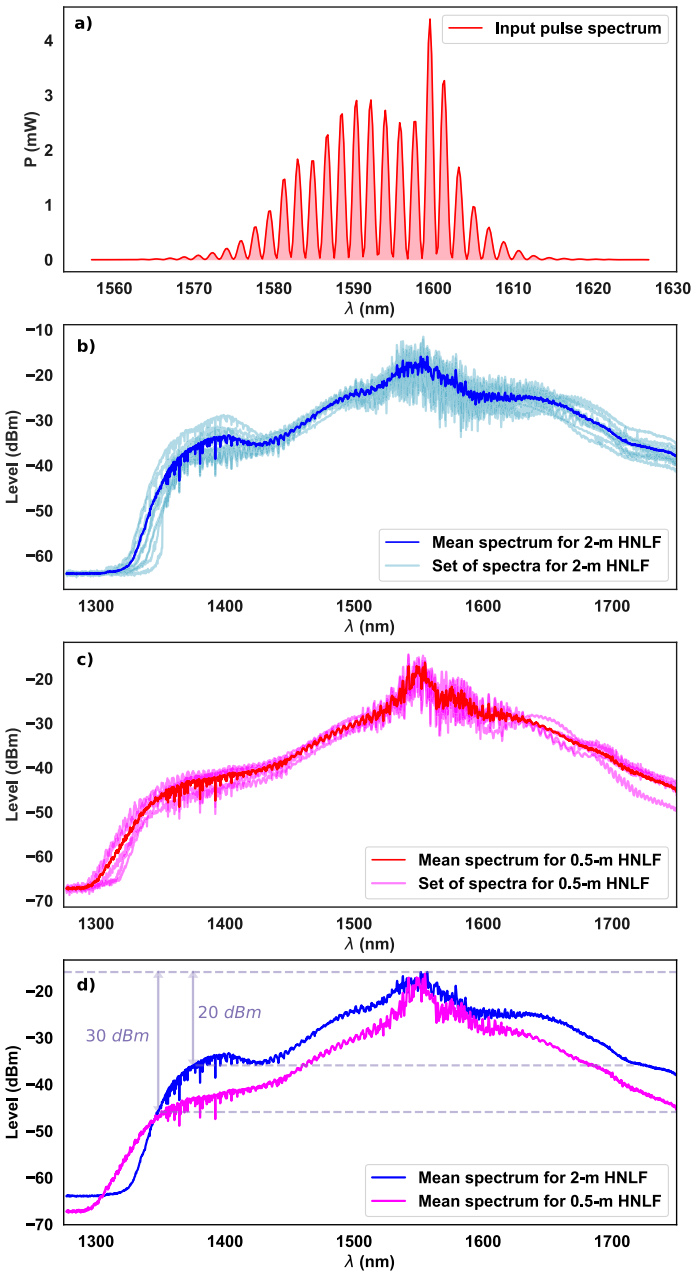

Fig. 13. (a) Input pulse spectral profile (linear scale), spectral variation of the SC for HNLF lengths: (b) 0.5-m, (c) 2-m, and (c) comparison of average spectra.

reports regarding the polarization state or soliton profile influence of the input seed pulse into the SC generation. In this work, the SC response generation was studied using conventional Kelly and bound states solitons as seed pulses, being tunable mode-locking regimes in the laser cavity. According to our results, we observed that the SC generation showed a strong dependence on both the pumping power, EDFA gain and seed soliton pulse profile, as the main responsible to obtain the broadest SC according to the nonlinear characteristics of each assembly, also allowing us to investigate the SC dynamics as linked to SPM and its output polarization state.

Besides, the reported results revealed a complete overview of recent research regarding the generation of mode-locked solitons by the use of topological insulators as Bi_2Se_3 with extraordinary optical properties such as high optical transmittance (>95%), high damage threshold (5 times higher than commercial SESAM), high modulation depth (46.5%), high signal-to-noise parameter (81.73) and high output power (38.26 mW) [62]. In another work, they reported the ultrashort pulse generation with 116.9 mW output power and 92.3 nm bandwidth by using a 2D ternary transition metal dicholcogenides $Nb_xRe_{(1-x)}S_2$ as SA [63]. Clearly, these new materials have shown enormous potential for both ML and SC applications.

Regarding our ML results using graphene SA, we could obtain a better performance in terms of output power, SNR and bandwidth when compared to those of Niobium telluride($NbTe_2$) [64] and Chromium oxide (Cr2O3) [65]. Some of the main characteristics of the mentioned references are shown in the Table 7 including the characterization of the vector solitons (VS) obtained with samples G_{98} and G_{65} (figure S9).

Table 6
Comparison between the reported seed EDFLs and their SC measurements.

Ref.	Fiber configuration	Seed EDFL parameters		SC generation parameters		
		SA material	$\Delta\lambda$ (nm)	NL fiber	Length (m)	$\Delta\lambda_{max}$ (nm)
[46]	–	NPR	35	HNLF	100	290 (−3 dB)
[47]	–	–	–	HNLF	0.2	1200 (−20 dB)
[48]	Optical connector tip	NPR+SAM	–	HNLF	600	1280 (−20 dB)
[49]	–	NPR	13.1	HNLF	1	600 (−20 dB)
[50]	Optical connector tip	CNT	16	HNLF	100	1000 (−30 dB)
[51]	Optical connector tip	CNT	10.1	HNLF	2	1200 (−20 dB)
[52]	Optical connector tip	LPE-Graphene	1.46	HNLF	100	400[a] (−20 dB)
[53]	–	NPR	–	HNLF	1	1360 (−20 dB)
[54]	–	NPR	30	–	–	410 (−30 dB)
[55]	Optical connector tip	Graphene	–	HNLF	0.73	1100 (−30 dB)
[56]	Optical connector tip	CNT	5.3	ZBLAN	10	420 (−20 dB)
[57]	–	Oscillator	–	HNLF	2	1380 (−−)
[58]	Optical connector tip	CNT	5	ZBLAN	25	2000 (−20 dB)
[59]	Optical connector tip	CNT	5	PCF	60	1050 (−20 dB)
[60]	Optical connector tip	CNT	5	HNLF	1000; 1	1000;1400 (−20 dB)
[61]	D-shaped fiber	Graphene	14.5	HNLF	2	288 (−20 dB)
Our work	D-shaped fiber	Graphene	11.6	HNLF/ZBLAN	2; 5	402[a]; 286[a] (−30 dB)

[a] Limited by the optical spectrum analyzer detection range.

Table 7
Comparative performance of mode-locked vector solitons as a function of SA.

SA	P_{pump} (mW)	P_{mean} (mW)	SNR (dB)	$\Delta\lambda$ (nm)	RR (MHz)	VS type	Authors	Ref.
$NbTe_2$	45–138	0.18–0.86	54	3.29	6.68	Pol-locked	X. Shang et al.	[64]
Bi_2Se_3	630	38.26	81.73	32.5	54.82	–	X. Xing et al.	[62]
$Nb_xRe_{(1-x)}S_2$	620–900	75.65 –116.9	77	92.3	35.6	Pol-locked	L. Li et al.	[63]
Cr_2O_3	580	–	65	10	34.48	–	L. Li et al.	[65]
PEA_2PbI_4 NCs	400	6.61	90	5.68	29.67	–	Y. He et al.	[66]
Graphene – G_{98}	79–267	0.8–2.7	71.7	14.1	36.21	Pol-locked	Our work	
Graphene – G_{65}	148–267	0.3–0.6	31.8	18.0	37.42			

4. Conclusions

We presented a study of supercontinuum generation from a mode-locked EDFL based on a monolayer graphene saturable absorber onto the polished surface of a D-shaped fiber using HNLF and ZBLAN. By introducing different input pulse spectrum profiles in the EDFA, spectral characterization showed a blue shift as a function of the amplifier gain, shifting the central wavelength of the output spectrum by 6.9 nm at 12 dB as directly influenced by gain dispersion, spontaneous emission, and modulation instability. In SC setup-1, the spectrum reached a maximum broadening at 11 and 13 dB of amplifier gain for 2-m HNFL and 5-m ZBLAN, respectively. However, the spectral broadening was reduced for higher gain values due to the high dependence on the polarization state of the input pulse spectrum into the EDFA and the nonlinear fibers. Therefore, the maximum SC was estimated by employing the 20-dBm spectral width, which resulted in 350 and 245 nm bandwidths for HNFL and ZBLAN, respectively, presenting more symmetric broadening in HNLF fiber concerning the input pulse spectrum. In setup-2, we generated SC bandwidths of 351 and 227 nm at 20-dBm for 2-m and 0.5-m HNLF lengths, respectively. Furthermore, spectral brightness was increased by (5.0 ± 1.8) dBm using the 2-m long HNLF. It is important to note that using an external PC allowed the adjustment of both broadening and brightness parameters of the resulting SC for higher operational EDFA gains in the system. In this way, a mean standard deviation in the spectral brightness of 1.3 and 0.5 μW for 2 and 0.5 -m HNLF lengths, respectively, was quantified.

CRediT authorship contribution statement

D.H. Martínez-Suárez: Conceptualization, Formal analysis, Investigation, Methodology, Software, Writing – original draft, Writing – review & editing. **M.C.S. Araujo:** Conceptualization, Writing – review & editing. **D. Steinberg:** Conceptualization, Formal analysis, Investigation, Methodology, Resources, Supervision, Writing – review & editing. **L.A.M. Saito:** Conceptualization, Writing – review & editing. **E.A. Thoroh de Souza:** Supervision, Review, Funding acquisition. **J.D. Zapata:** Conceptualization, Funding acquisition, Investigation, Supervision, Writing & review.

Declaration of competing interest

The authors declare that they have no known competing financial interests or personal relationships that could have appeared to influence the work reported in this paper.

Data availability

The data set and code associated with this paper is available at SC-JOLT\robustify_110588.

Acknowledgments

The authors thank the GITA research group of the Faculty of Engineering of the University of Antioquia (Colombia) for facilitating the space in the Optics Laboratory to carry out the experiments and the Graphene and Nanotechnology Research Center (MackGraphe) of the Mackenzie Presbyterian University (Brazil) for the support. We also thank Andres Betancur from the Metropolitan Technological Institute (ITM) for help with the RF measurements.

Finally, we thank the reviewers and the editor of the journal.

Funding acknowledgments

This work was financially supported for the research by the Bicentennial Doctoral Excellence Scholarship Program - Cohort 2 of Minciencias (20230030-07-2021), CNPq - National Council for Scientific and Technological Development (142540/2019-6), MackPesquisa (231022), FAPESP - Sao Paulo Research Foundation (2022/08932-9), Universidad de Antioquia Fundacion – FUA from Universidad de Antioquia (G8-2020 1108 3906, 2022–55290) and University of Antioquia proyect (2023-58610).

Appendix A. Supplementary data

Supplementary material related to this article can be found online at https://doi.org/10.1016/j.optlastec.2024.110588.

References

[1] J. Ma, Z. Qin, G. Xie, L. Qian, D. Tang, Review of mid-infrared mode-locked laser sources in the 2.0 μm – 3.5 μm spectral region, Appl. Phys. Rev. 6 (2019) 21317, http://dx.doi.org/10.1063/1.5037274.

[2] C.R. Petersen, N. Prtljaga, M. Farries, J. Ward, B. Napier, G.R. Lloyd, J. Nallala, N. Stone, O. Bang, Mid-infrared multispectral tissue imaging using a chalcogenide fiber supercontinuum source, Opt. Lett. 43 (2018) 999–1002, http://dx.doi.org/10.1364/OL.43.000999.

[3] H.J. Butler, P.M. Brennan, J.M. Cameron, D. Finlayson, M.G. Hegarty, M.D. Jenkinson, D.S. Palmer, B.R. Smith, M.J. Baker, Development of high-throughput ATR-FTIR technology for rapid triage of brain cancer, Nature Commun. 10 (2019) 1–9, http://dx.doi.org/10.1038/s41467-019-12527-5.

[4] I. Suzuki, M. Ogawa, K. Seino, M. Nogawa, H. Naito, K.I. Yamakoshi, S. Tanaka, Reagentless estimation of urea and creatinine concentrations using near-infrared spectroscopy for spot urine test of urea-to-creatinine ratio, Adv. Biomed. Eng. 7 (2018) 72–81, http://dx.doi.org/10.14326/abe.7.72.

[5] C.R. Petersen, U. Møller, I. Kubat, B. Zhou, S. Dupont, J. Ramsay, T. Benson, S. Sujecki, N. Abdel-Moneim, Z. Tang, D. Furniss, A. Seddon, O. Bang, Mid-infrared supercontinuum covering the 1.4–13.3 μm molecular fingerprint region using ultra-high NA chalcogenide step-index fibre, Nat. Photon. 8 (2014) 830–834, http://dx.doi.org/10.1038/nphoton.2014.213.

[6] E. Belykh, K. Yagmurlu, N. Martirosyan, T. Lei, M. Izadyyazdanabadi, K. Malik, Laser application in neurosurgery, Surg. Neurol. Int. 8:274 (2018) http://dx.doi.org/10.4103/sni.sni_489_16.

[7] X. Liu, Q. Gao, Y. Zheng, D. Mao, J. Zhao, Recent progress of pulsed fiber lasers based on transition-metal dichalcogenides and black phosphorus saturable absorbers, Nanophotonics 9 (2020) 2215–2231, http://dx.doi.org/10.1515/nanoph-2019-0566.

[8] H. Ahmad, S. Reduan, N. Yusoff, M. Ismail, S. Aidit, Mode-locked pulse generation in erbium-doped fiber laser by evanescent field interaction with reduced graphene oxide-titanium dioxide nanohybrid, Opt. Laser Technol. 118 (2019) 93–101, http://dx.doi.org/10.1016/j.optlastec.2019.05.015.

[9] A. Marini, J.D. Cox, F.J. Garc, Theory of graphene saturable absorption, 125408, 2017, 1–11. http://dx.doi.org/10.1103/PhysRevB.95.125408.

[10] X. Li, D. Wang, K. Hua, Q. Chen, Y. Ge, Q. Xia, Saturable absorber based on graphene for a hybrid passive mode-locked erbium-doped fiber laser, Opt. Fiber Technol., Mater. Devices Syst. 70 (2022) 102867, http://dx.doi.org/10.1016/j.yofte.2022.102867.

[11] U. Keller, K.J. Weingarten, F.X. Kartner, D. Kopf, B. Braun, I.D. Jung, R. Fluck, C. Honninger, N. Matuschek, J. der Au, Semiconductor saturable absorber mirrors (SESAM's) for femtosecond to nanosecond pulse generation in solid-state lasers, IEEE J. Sel. Top. Quantum Electron. 2 (1996) 435–453, http://dx.doi.org/10.1109/2944.571743.

[12] D. Steinberg, L. Saito, H. Rosa, E. Thoroh de Souza, Single-walled carbon nanotube passively mode-locked O-band Raman fiber laser, Opt. Laser Technol. 79 (2016) 55–61, http://dx.doi.org/10.1016/j.optlastec.2015.11.012.

[13] U. Keller, Recent developments in compact ultrafast lasers, Nature 424 (2003) 831–838.

[14] A.H. Castro, F. Guinea, N.M. Peres, K.S. Novoselov, A.K. Geim, The electronic properties of graphene, Rev. Modern Phys. 81 (2009) 109–162, http://dx.doi.org/10.1103/RevModPhys.81.109.

[15] A. Malouf, O. Henderson-Sapir, S. Set, S. Yamashita, D.J. Ottaway, Two-photon absorption and saturable absorption of mid-IR in graphene, Appl. Phys. Lett. 114 (2019) 91111, http://dx.doi.org/10.1063/1.5088641.

[16] F. Bonaccorso, Z. Sun, T. Hasan, A.C. Ferrari, Graphene photonics and optoelectronics, Nat. Photon. 4 (2010) 611–622, http://dx.doi.org/10.1038/nphoton.2010.186.

[17] K.Y. Lau, N.H.Z. Abidin, M.H.A. Bakar, A.A. Latif, F.D. Muhammad, N.M. Huang, M.F. Omar, M.A. Mahdi, Passively mode-locked ultrashort pulse fiber laser incorporating multi-layered graphene nanoplatelets saturable absorber, J. Phys. Commun. 2 (2018) 75005, http://dx.doi.org/10.1088/2399-6528/aacdbe.

[18] D. Steinberg, J.D. Zapata, L.A.M. Saito, E.A. Thoroh de Souza, Study of pulse formation in an EDFL under a large dispersion variation hybridly mode-locked by graphene and nonlinear polarization rotation, IEEE Photonics J. 13 (2021) 1–14, http://dx.doi.org/10.1109/JPHOT.2021.3061519.

[19] J.D. Zapata, D. Steinberg, L.A.M. Saito, E.A. Thoroh de Souza, Ultrashort pulse generation performance in short and ultralong EDFL cavities using CVD monolayer graphene, Optica Publishing Group, 2018, p. W2D.2, http://dx.doi.org/10.1364/LAOP.2018.W2D.2,

[20] G.X. Liu, D.J. Feng, M.S. Zhang, S.Z. Jiang, C. Zhang, Mode-locked erbium-doped all fiber laser using few-layer graphene as a saturable absorber, Opt. Laser Technol. 72 (2015) 70–73, http://dx.doi.org/10.1016/j.optlastec.2015.02.006.

[21] X. Wang, W. Ma, Y. Fu, X. Liu, Z. Tao, Y. Song, K. Dong, H. Jiang, Two-dimensional material integrated micro-nano fiber, the new opportunity in all-optical signal processing, Nanophotonics 12 (12) (2023) 2073–2101, http://dx.doi.org/10.1515/nanoph-2023-0223.

[22] N. An, C. Qin, Y. Li, T. Tan, Z. Yuan, H. Zhang, Y. Wu, B. Yao, Y. Rao, Graphene-fiber biochemical sensors: Principles, implementations, and advances, Photon. Sens. 11 (2021) 123–139, http://dx.doi.org/10.1007/s13320-021-0617-6.

[23] X. Zhou, Q. Deng, W. Yu, K. Liu, Z. Liu, The rise of graphene photonic crystal fibers, Adv. Funct. Mater. 32 (42) (2022) 2202282, http://dx.doi.org/10.1002/adfm.202202282.

[24] Y. Zhang, L. Zhou, D. Qiao, M. Liu, H. Yang, C. Meng, T. Miao, J. Xue, Y. Yao, Progress on optical fiber biochemical sensors based on graphene, Micromachines 13 (3) (2022) http://dx.doi.org/10.3390/mi13030348.

[25] D.H. Martínez-Suárez, M.C.S. Araujo, D. Steinberg, J.B. Martínez, L.A.M. Saito, E.A. Thoroh de Souza, J.D. Zapata, Power, polarization, and spectrum mapping of a mode- locked erbium-doped fiber laser using a motorized adaptive polarization controller (MAPOC), in: Frontiers in Optics + Laser Science 2022, (FIO, LS), Optica Publishing Group, 2022, p. JW5B.12, http://dx.doi.org/10.1364/FIO.2022.JW5B.12.

[26] M.I. Hasan, N. Akhmediev, W. Chang, Mid-infrared supercontinuum generation in supercritical xenon-filled hollow-core negative curvature fibers, Opt. Lett. 41 (2016) 5122–5125, http://dx.doi.org/10.1364/OL.41.005122.

[27] N. Granzow, Supercontinuum white light lasers: a review on technology and applications, in: M. Rosenberger, P.-G. Dittrich, B. Zagar (Eds.), in: Photonics and Education in Measurement Science 2019, Vol. 11144, SPIE, International Society for Optics and Photonics, 2019, 1114408, http://dx.doi.org/10.1117/12.2533094.

[28] R.I. Woodward, E.J.R. Kelleher, 2D saturable absorbers for fibre lasers, Appl. Sci. 5 (2015) 1440–1456, http://dx.doi.org/10.3390/app5041440.

[29] F. Gallazzi, I. Cáceres, L. Monroy, J. Nuño, C. Pulido, P. Corredera, F.B. Naranjo, M. González-Herráez, J.D.A. Castañón, Ultralong ring laser supercontinuum sources using standard telecommunication fibre, Opt. Laser Technol. 147 (2022) 107632, http://dx.doi.org/10.1016/j.optlastec.2021.107632.

[30] S.K. Jain, R. Sharma, P. Amrit, V.K. Chandna, G. Sharma, A.K. Yadav, S. Vyas, Semiconductor material photonic crystal fiber for mid-infrared supercontinuum generation, Mater. Today: Proc. 74 (2023) 255–258, http://dx.doi.org/10.1016/j.matpr.2022.08.117, International Conference on Advances in Materials Science, Communication and Microelectronics.

[31] G.A. Newburgh, M. Dubinskii, Power and efficiency scaling of Er: ZBLAN fiber laser, Laser Phys. Lett. 18 (2021) 95102, http://dx.doi.org/10.1088/1612-202x/ac1608.

[32] S.M. Salimullah, M. Faisal, Ultra-wideband and coherent supercontinuum generation (near and mid-infrared) in dispersion flattened ZnGeP2 photonic crystal fiber, Alex. Eng. J. 70 (2023) 289–300, http://dx.doi.org/10.1016/j.aej.2023.03.002.

[33] L. Chu Van, K. Dinh Xuan, T. Le Canh, T. Thai Doan, T. Nguyen Thi, H. Van Le, V.T. Hoang, Supercontinuum generation in chalcogenide photonic crystal fiber infiltrated with liquid, Opt. Mater. 137 (2023) 113547, http://dx.doi.org/10.1016/j.optmat.2023.113547.

[34] S. Venck, F. St-Hilaire, L. Brilland, A.N. Ghosh, R. Chahal, C. Caillaud, M. Meneghetti, J. Troles, F. Joulain, S. Cozic, S. Poulain, G. Huss, M. Rochette, J.M. Dudley, T. Sylvestre, 2–10 μm mid-infrared fiber-based supercontinuum laser source: Experiment and simulation, Laser Photonics Rev. 14 (2020) 2000011, http://dx.doi.org/10.1002/lpor.202000011.

[35] M. Liu, Z.W. Wei, A.P. Luo, W.C. Xu, Z.C. Luo, Recent progress on applications of 2D material-decorated microfiber photonic devices in pulse shaping and all-optical signal processing, Nanophotonics 9 (2020) 2641–2671, http://dx.doi.org/10.1515/nanoph-2019-0564.

[36] G. Sobon, Application of 2D materials to ultrashort laser pulse generation, in: Two-dimensional Materials - Synthesis, Characterization and Potential Applications, InTech, 2016, http://dx.doi.org/10.5772/63336.

[37] L. Zhao, Vector dissipative solitons, in: M.F.S. Ferreira (Ed.), Dissipative Optical Solitons, Springer International Publishing, Cham, 2022, pp. 105–130, http://dx.doi.org/10.1007/978-3-030-97493-0_6.

[38] N. VS, R. T, S. Kempahanumakkagari, P. HR, P. BM, Efficient strategies to produce graphene and functionalized graphene materials: A review, Appl. Surf. Sci. Adv. 14 (2023) 100386, http://dx.doi.org/10.1016/j.apsadv.2023.100386.

[39] P. Glas, D. Fischer, G. Steinmeyer, A. Husakou, J. Herrmann, R. Iliew, N.B. Skibina, V.I. Beloglasov, Y.S. Skibina, Supercontinuum generation in a two-dimensional photonic kagome crystal, Appl. Phys. B 81 (2005) 209–217, http://dx.doi.org/10.1007/s00340-005-1847-9.

[40] S.S. Bobba, A. Agrawal, Ultra-broad mid-IR supercontinuum generation in single, Bi and Tri layer graphene nano-plasmonic waveguides pumping at low input peak powers, Sci. Rep. 7 (2017) 10192, http://dx.doi.org/10.1038/s41598-017-10141-3.

[41] J.M. Dudley, J.R. Taylor, Supercontinuum Generation in Optical Fibers, Cambridge University Press, Cambridge, 2010.

[42] J.D. Zapata, D. Steinberg, L.A.M. Saito, R.E.P. de Oliveira, A.M. Cárdenas, E.A. Thoroh de Souza, Efficient graphene saturable absorbers on D-shaped optical fiber for ultrashort pulse generation, Sci. Rep. 6 (2016) 20644, http://dx.doi.org/10.1038/srep20644.

[43] G. Agrawal, Applications of Nonlinear Fiber Optics, Elsevier, 2001.
[44] G. Agrawal, in: G. Agrawal (Ed.), Chapter 13 - Supercontinuum Generation, fifth ed., Academic Press, Boston, 2013, pp. 553–612, http://dx.doi.org/10.1016/B978-0-12-397023-7.00013-9.
[45] A.P. Luo, H. Liu, N. Zhao, X.W. Zheng, M. Liu, R. Tang, Z.C. Luo, W.C. Xu, Observation of three bound states from a topological insulator mode-locked soliton fiber laser, IEEE Photonics J. 6 (2014) 1–8, http://dx.doi.org/10.1109/JPHOT.2014.2345874.
[46] H. Ahmad, A. Latif, N. Awang, M. Zulkifli, K. Thambiratnam, Z. Ghani, S. Harun, Wide-band fanned-out supercontinuum source covering O-, E-, S-, C-, L- and U-bands, Opt. Laser Technol. 44 (7) (2012) 2168–2174, http://dx.doi.org/10.1016/j.optlastec.2012.03.007.
[47] Y. Nomura, Y. Nozaki, Y. Sakakibara, E. Omoda, H. Kataura, N. Nishizawa, Octave spanning coherent supercontinuum generation by 46 fs pedestal free ultrashort pulse using similariton amplifier and Er-doped fiber laser with carbon nanotube, in: CLEO: 2014, Optica Publishing Group, 2014, p. STh3N.5, http://dx.doi.org/10.1364/CLEO_SI.2014.STh3N.5.
[48] S. Kim, J. Park, S. Han, Y.-J. Kim, S.-W. Kim, Coherent supercontinuum generation using Er-doped fiber laser of hybrid mode-locking, Opt. Lett. 39 (10) (2014) 2986–2989, http://dx.doi.org/10.1364/OL.39.002986.
[49] S. Lin, S.-K. Hwang, J.-M. Liu, Supercontinuum generation in highly nonlinear fibers using amplified noise-like optical pulses, Opt. Express 22 (4) (2014) 4152–4160, http://dx.doi.org/10.1364/OE.22.004152.
[50] S.N.M. Rifin, M.Z. Zulkifli, S.N.M. Hassan, Y. Munajat, H. Ahmad, Broadband supercontinuum generation with femtosecond pulse width in erbium-doped fiber laser (EDFL), Laser Phys. 26 (11) (2016) 115102, http://dx.doi.org/10.1088/1054-660X/26/11/115102.
[51] N. Nishizawa, T. Niinomi, Y. Nomura, L. Jin, Y. Ozeki, Octave spanning coherent supercontinuum comb generation based on Er-doped fiber lasers and their characterization, IEEE J. Sel. Top. Quantum Electron. 24 (3) (2018) 1–9, http://dx.doi.org/10.1109/JSTQE.2017.2776521.
[52] Y.I. Hammadi, T.S. Mansour, I.A.M. Alani, M.H.M. Ahmed, Z. Jusoh, E. Engineering, Graphene based soliton mode-locked erbium doped fiber laser for supercontinuum generation, 13, 2018, 777–784.
[53] K.Y. Chang, W.C. Chen, S.S. Lin, S.K. Hwang, J.M. Liu, High-power, octave-spanning supercontinuum generation in highly nonlinear fibers using noise-like and well-defined pump optical pulses, OSA Contin. 1 (3) (2018) 851–863, http://dx.doi.org/10.1364/OSAC.1.000851.
[54] Y.X. Guo, X.H. Li, P. lai Guo, H. Zheng, Supercontinuum generation in an Er-doped figure-eight passively mode-locked fiber laser, Opt. Express 26 (8) (2018) 9893–9900, http://dx.doi.org/10.1364/OE.26.009893.
[55] K. Tarnowski, T. Martynkien, P. Mergo, J. Sotor, G. Soboń, Compact all-fiber source of coherent linearly polarized octave-spanning supercontinuum based on normal dispersion silica fiber, Sci. Rep. 9 (2019) 12313, http://dx.doi.org/10.1038/s41598-019-48726-9.
[56] H. Liu, Y. Yu, W. Song, Q. Jiang, F. Pang, T. Wang, Spectrally flat supercontinuum generation in a ZBLAN fiber pumped by erbium-doped mode-locked fiber laser, Photon. Sens. 9 (2019) 302–308, http://dx.doi.org/10.1007/s13320-019-0552-y.
[57] S.T. Fan, Y.Y. Zhang, L.L. Yan, W.G. Guo, S.G. Zhang, H.F. Jiang, Supercontinuum generation of highly nonlinear fibers pumped by 1.57-μm laser soliton, Chin. Phys. B 28 (6) (2019) 064204, http://dx.doi.org/10.1088/1674-1056/28/6/064204.
[58] S.R. Yemineni, W.J. Lai, A. Arokiaswami, P. Shum, Mid-IR supercontinuum generation in a single-mode ZBLAN fiber pumped by a carbon-nanotube-based passively mode-locked erbium-doped femtosecond fiber laser, in: K.L. Vodopyanov, K.L. Schepler (Eds.), in: Nonlinear Frequency Generation and Conversion: Materials and Devices XVII, Vol. 10516, SPIE, International Society for Optics and Photonics, 2018, 105160N, http://dx.doi.org/10.1117/12.2285315.
[59] S.R. Yemineni, W.J. Lai, A. Arokiaswami, P. Shum, Broadband supercontinuum generation in photonics crystal fiber pumped by femtosecond carbon-nanotube-based passively mode-locked erbium-doped fiber laser, in: 2017 Progress in Electromagnetics Research Symposium - Fall, (PIERS - FALL), 2017, pp. 2993–2995, http://dx.doi.org/10.1109/PIERS-FALL.2017.8293647.
[60] S.R. Yemineni, W.J. Lai, A. Arokiaswami, P. Shum, Flat broadband supercontinuum generation in a short length of highly nonlinear fiber pumped by a femtosecond carbon-nanotube based passively mode-locked erbium-doped fiber laser, in: K.L. Vodopyanov, K.L. Schepler (Eds.), in: Nonlinear Frequency Generation and Conversion: Materials and Devices XVII, Vol. 10516, SPIE, International Society for Optics and Photonics, 2018, 105160A, http://dx.doi.org/10.1117/12.2283385.
[61] S. Castrillón, A. Ospina, D.H. Martínez-Suárez, J.F. Botía, J.D. Zapata, A strong correlation between power and spectrum bandwidth in a supercontinuum based on monolayer graphene, in: Frontiers in Optics + Laser Science 2022 (FIO, LS), Optica Publishing Group, 2022, p. JW5B.21, http://dx.doi.org/10.1364/FIO.2022.JW5B.21,
[62] X. Xing, Y. Liu, J. Han, W. Liu, Z. Wei, Preparation of high damage threshold device based on Bi2Se3 film and its application in fiber lasers, ACS Photon. 10 (7) (2023) 2264–2271, http://dx.doi.org/10.1021/acsphotonics.2c01375.
[63] L. Li, L. Pang, R. Wang, X. Zhang, Z. Hui, D. Han, F. Zhao, W. Liu, Ternary transition metal dichalcogenides for high power vector dissipative soliton ultrafast fiber laser, Laser Photonics Rev. 16 (2) (2022) 2100255, http://dx.doi.org/10.1002/lpor.202100255.
[64] X. Shang, N. Xu, J. Guo, S. Sun, H. Zhang, S. Wageh, A.A. Al-Ghamdi, H. Zhang, D. Li, Niobium telluride absorber for a mode-locked vector soliton fiber laser, Sci. China Phys. Mech. Astron. 66 (2023) 254211, http://dx.doi.org/10.1007/s11433-022-2058-3.
[65] L. Li, J. Cheng, Q. Zhao, J. Zhang, H. Yang, Y. Zhang, Z. Hui, F. Zhao, W. Liu, Chromium oxide film for Q-switched and mode-locked pulse generation, Opt. Express 31 (10) (2023) 16872–16881, http://dx.doi.org/10.1364/OE.491792.
[66] Y. He, N. Li, Y. Feng, X. Li, D. Liu, J. Huang, R. Zhou, M. Wu, L. Miao, C. Zhao, Broadband nonlinear optical modulator with 2D organic-inorganic hybrid perovskite nanocrystals, IEEE J. Sel. Top. Quantum Electron. 29 (6: Photonic Signal Processing) (2023) 1–8, http://dx.doi.org/10.1109/JSTQE.2023.3253566.